

A DEEP LEARNING METHOD TO PREDICT OUTDOOR TEMPERATURE PROFILE OF PAVEMENT BRICKS WITH PHASE CHANGE MATERIALS

CHIEN HWA CHONG^{1,*}, JASON Y. S. LOO², DARRELL J.J. YAP²,
ZI JUN CHAN², MUHAMMAD ABUBAKAR², SHANAHAN A/L SURESH²,
ALI WAEEL MOHAMED ALI ELLEITHY², WEI LIANG GAN², WEI HAN
TAN¹, WAN THING HONG³, TOMAS MAUL²

¹Department of Chemical and Environmental Engineering, Faculty of Science and
Engineering, University of Nottingham, Jalan Broga, Semenyih 43500, Malaysia

²School of Computer Science, University of Nottingham Malaysia, 43500 Selangor, Malaysia

³School of Energy, Geoscience, Infrastructure and Society, Heriot-Watt University
Malaysia, 62200 Putrajaya, Malaysia

*Corresponding Author: ChienHwa.Chong@nottingham.edu.my

Abstract

Urban heat islands are one of the common issues of the 21st century. Phase change materials could potentially minimise the impact of the urban heat island. There is growing interest in using phase change material (PCM) incorporated bricks for building materials and the results so far have been promising. The objective of this study was to evaluate the temperature profiles of phase change materials, develop a corresponding machine learning dataset, and design a deep learning method to predict temperature profiles from PCM variables. The phase change materials selected in this study were lauric acids, stearic acids, and paraffin wax. The normalized data was split into a training set and a test set with a ratio of 9:1. Further to this, for the purpose of training the model, the original heatmap images were resized to a dimension of 160 x 120 pixels. The mean squared error between heat maps from the test set and corresponding predictions was computed, yielding an error of 0.0465, which is consistent with the viability of the approach. This work demonstrates that deep learning models based on fully connected and convolutional layers are capable of accurately predicting heat maps from PCM variables, even when relatively small datasets are used, and therefore that they are a good place to start for authors conducting similar work.

Keywords: Machine learning, Modelling, Phase change materials, Temperature profile.

1. Introduction

Urbanisation and industrialisation promote anthropogenic activities, which increase the total heat energy input in the area which is reflected in the upward trend of the global annual temperature since the preindustrial period. Increasing global temperature has threatened the population in urban areas the most. Urban expansion has introduced man-made structures, and enhanced building and population densities, which have caused a surge in vehicle numbers and energy demands. Consequently, we have witnessed a drastic increase in overall heat emissions, and a disruption of the initial balanced heat energy system. This phenomenon is known as the urban heat island (UHI) effect where urban areas have an average temperature that is greater than rural areas. The main novel contributions of this work consist of: (1) an experimental setup involving pavement bricks incorporated with phase change materials (PCMs) with different combinations of paraffin wax, stearic acids, and lauric acids, (2) a corresponding dataset associating physical variables relevant to the experimental setup and resulting heat maps, (3) a deep learning proof of concept capable of predicting heat maps from the physical variables defined in the dataset. The following sub-sections summarize the key related works underlying these contributions.

1.1. Principle of urban heat island

Heat from solar radiation is the primary heat source while anthropogenic activities are the secondary heat contributor. The modification of the landscape is the main cause of the UHI effect since man-made structures and dark surfaces absorb heat during the daytime and release heat at night. The geometrical design of modern buildings contributes to trapping heat energy and acts as a heat sink. Tall buildings not only reflect and absorb heat energy within the lower regions of urban areas, but it also inhibits natural convection cooling from wind flow, a phenomenon which is called the urban canyon effect. On top of that, the waste heat generated from exhaust pipes amplifies the UHI effect. Airflow congestion causes pollutants to reside in the air and affects the radiative properties of the atmosphere. Additional heat stores in man-made structures are released during the nighttime which increases the surrounding temperature and results in the largest temperature difference with surrounding rural areas throughout the day [1].

UHI uncontrollable variables consist of natural events while controllable UHI variables involve urban landscape design. The population directly impacts the heat released from anthropogenic activities and urban design aspects, such as sky view factors, green areas, and building materials, affect the amount of heat trapped in urban areas.

1.2. Impact of urban heat island

Exposure to high temperatures will exacerbate minor existing health conditions and even pose the risk of hospitalisation and death. Temperature increments due to UHI, increases heat-related mortality risk, and this is likely to increase due to the worsening of climate change in the future. In high-income neighbourhoods, air conditioning is widely used to reduce heat vulnerability. This causes socio-economic inequalities as low-income communities typically cannot afford air conditioning unless it is heavily subsidised by the government. Exacerbating energy consumption to reduce the surrounding temperature is commonly practised in our daily life, for instance, in

active cooling systems [2]. Other than that, Wong et al. [3] conducted a survey of up to 1050 participants from the working community in Kuala Lumpur, Malaysia. Kuala Lumpur as a megacity is experiencing UHI, whereby the working community suffers from physical, psychological, and social health challenges. The working community in Kuala Lumpur tends to experience respiratory illness the most (90.2%) and heat exhaustion next (83.1%). On top of that, the heat effect has caused 64.7% of the survey participants to fall into depression and up to 90.6% reduced outdoor activities due to the extreme temperature. Therefore, control measures and mitigation plans need to be implemented.

1.3. Passive cooling materials as UHI mitigation technique

Material is an essential component in passive cooling systems since it possesses significant factors in determining temperatures of both horizontal and vertical built surfaces. To improve the urban microclimate and outdoor thermal comfort conditions, several types of cool materials have been recently studied and applied in a wide variety of climates and places. Among the currently researched UHI mitigation techniques, cool surfaces and green spaces are identified as the most effective ways in reducing surface overheating, building cooling energy consumption and CO₂ emissions in the atmosphere. Although the use of greeneries on the roof and building façades contributes to both cooling effects and aesthetic values, cool materials are simpler to implement in terms of technology and usually easier to be maintained.

Active research on passive cooling materials and their intrinsic thermal resistance properties has provided evidence for the importance of advanced cooling materials. Materials such as insulations, high-albedo coatings for building envelopes, evaporative cooling walls, radiative cooling roof, and cooling paving, are part of recent research developments. Another effective and modern technique used to mitigate the UHI effect consists of PCM incorporated materials. Incorporating PCMs with construction materials is an advanced technology, owing to their enhancement potential for heat storage and heat release during phase transition. The inclusion of both thermal insulation and PCM provides a significant reduction of energy consumption and undesired thermal load, but the PCM reduces further this consumption when the thermal level and range melting temperature are appropriate i.e., melting temperature slightly higher than a comfort temperature, associated with an adequate melting range. Although PCM technology has shown a remarkable enhancement of building thermal energy properties in building façades, less attention has been given to the incorporation of PCMs in horizontal built surfaces such as roofs and pavements [4]. This is especially important for outdoor thermal comfort as heat convection of horizontal surfaces is higher than vertical surfaces under ambient air conditions. As pavements are used to create urban spaces and footpaths, the types of materials used will significantly influence the pedestrians' thermal comfort levels. This has been studied by Djekic et al. [5], Manteghi et al. [6], and Taleghani and Berardi [7] on the types of pavement materials that affect the microclimate thermal comfort and heating up of pedestrian surfaces in public open spaces in the context of contemporary urban design.

1.4. Recent research development on PCM materials

Saxena et al. [8] conducted an experiment on evaluating the heat transfer performance of PCM incorporated brick. The brick used has a dimension of 22.5 cm x 12 cm x 10

cm and 1.7 cm thickness and 16 cm length for the PCM slot. It is reported that the dual PCM layer brick is able to reduce the temperature by up to 9.5°C with 60% reduction in heat gain with Eicosane and OM 35 in each slot. Alawadhi [9] also conducted an experiment on the impact of PCM on indoor brick surfaces. The location and quantity of PCM has also been studied. It is reported that PCM integration will reduce heat gains in bricks thus preventing the heat to reach the indoor space. A positive effect can be observed as the quantity of PCM increases. The centreline of the brick as the location for PCM shows the best performance and the strength of the brick is not compromised. The PCM used by Alawadhi [9] is the n-eicosane which shows a heat flux reduction of up to 17.55% on the indoor brick surface. On top of that, a numerical simulation study by Arunkumar *et al.* [10] also shows a positive result with PCM incorporated bricks. The geometry of the brick is 40 cm x 10 cm x 20 cm with a hollow cavity of 12 cm x 16 cm x 40 cm. The setup showed a temperature drop of about 2°C (5.7%) and a heat gain reduction of 33% using Organic Material (OM) 29 PCM. Kumar *et al.* [11] studied the temperature profile of a test room with PCM integrated bricks. A test room with 3 m x 3 m x 3.65 m dimension was built with 20 cm x 20 cm x 40 cm sized bricks with 12 holes of size 5.3 cm x 3 cm x 40 cm. The PCM used consisted of calcium chloride hexahydrate, caesium, and tin chloride. It was reported that a maximum room temperature reduction of 6°C and a minimum of below 2°C was achieved. However, in a numerical simulation done on DESIGN BUILDER, the simulated values were about 4 °C for the room temperature reduction. Aketouane *et al.* [12] did a calculation on the potential energy savings by using the PCM integrated brick. It was reported that with a 27°C melting temperature PCM, 40% savings could be achieved. The calculation was done using data from Morocco.

PCM incorporated bricks show promising results from absorbing heat from the outdoors and cooling the indoor surface of a building. However, the performance of PCM incorporated bricks is not linear with the PCM quantity consumed in a pavement application. Athukorallage *et al.* [13] incorporated PCM in asphalt concrete pavement to study the impacts of PCM quantity. It was reported that PCM embedded pavement has a higher surface temperature compared to the pavement without PCM when the PCM volume fraction is above 60%. This is due to the reduced heat transfer through the pavement caused by the lower thermal conductivity of the melted PCM. Besides, Refaa *et al.*, [14] evaluated the impact of thermal conductivity enhancement, whereby a positive result was observed in terms of pavement temperature gradient. However, PCM impregnated pavement tends to have weaker physical properties which cause rutting [15-17].

As mentioned above, the three controllable UHI variables are sky view factor, green areas, and building materials. In this paper, the key focus rests on building materials. The properties of a brick affect its heat gain which directly affects the adjacent surrounding temperature. PCM impregnation shows promising results in reducing the heat gain of bricks, however, the thermal conductivity of the selected phase change material (PCM) is the key component. A low thermal conductivity PCM delays the heat reduction of the brick which is one of the key challenges. Although it is obvious that the potential of PCM impregnated bricks is significant in the context of buildings, studies on pavements made from PCM incorporated bricks are rare. The surrounding temperatures of walkways in the garden, hospital outdoor areas, and sidewalks could be minimised with pavements with PCM incorporated bricks. This can encourage pedestrians to use walkways especially under hot weather

conditions, which are frequently experienced in Malaysia. Therefore, PCM incorporation in pavement bricks was investigated in this research. The PCMs selected in this study are paraffin wax, lauric acids and stearic acids. Paraffin wax is an alkane derived from petroleum waste products. It is one of the common PCMs used in the building and construction industry as it has a high heat of fusion per unit weight, has a large melting point selection, is non-corrosive, exhibits stable thermal cycling, is chemically inert and has low thermal conductivity. In addition, it also exhibits moderate volume changes from 10 to 20% during melting but has low vapor pressure [18]. Lauric acids, paraffin wax, and stearic acids have a suitable melting temperature and relatively high latent heat that make it possible for low-temperature thermal energy storage. For a passive PCM storage, a thermal energy storage depends on climatic conditions. Keles et al. [19] claimed that adjusting the melting temperature of PCM with the specific climate requirements or outdoor experiments can be done by setting binary or ternary mixtures of fatty acids. For example, a lauric and stearic acid mixture with a melting point of 37 and fusion heat of 182.7 J g⁻¹ was reported in [20].

1.5. Recent related deep learning works

Given that our problem corresponds essentially to learning a complex non-linear mapping from a set of unstructured and heterogeneous variables to images (i.e. heat maps), the research works most closely related to ours pertain to generative models. We surveyed the literature for potential generative approaches that would be effective in this mapping, whilst still being relatively compact and simple to interpret.

Given their prevalence and relative success as generative models, Generative Adversarial Networks (GANs), are an obvious candidate for the task. Refer to [21-24] for several recent reviews on GANs applied to the image domain. GANs simultaneously train two different models in a competitive manner, whereby a generative model, known as G, captures the data distribution and attempts to recreate images comparable to those fed in. This process takes place whilst a discriminative model, known as D, is tasked with deciphering the source of a given image to determine whether it originated from the training set data or was created by the G model. The most optimal solution for GANs is obtained when the G model is capable of completely capturing the training data distribution, making model D consistently perform at chance level, meaning that the images created by G are indistinguishable to those sourced from the training set. Although generic GANs are still a prolific area by themselves they are insufficient for our purposes since it is not enough to simply generate images according to some distribution. In our case what is needed is some way to associate unstructured variables with images.

Conditional GANs (CGANs) are a simple GAN extension [25-28] that can help with the above problem. CGANs are known to be GANs that integrate different labels into the input space that help contextualize the generative process and stabilise the GAN training procedure whilst also producing synthesized images that look more natural. In this paper, Wang et al. managed to discuss the possibility of incorporating CGANs for object segmentation that allowed users to add or remove objects and change object categories. One potential downside of this approach is that images can have poor resolution.

Another relevant GAN extension pertains to CookGAN, which is a deep learning model that undergoes training using an attention-based association method

[29]. The model functions by mapping a list of ingredients to its corresponding images in a joint latent space. The CookGAN input consists of 3 components: a) an ingredient list, b) corresponding output images, and c) fake output images. Two neural networks are trained to minimise the chance of a false image appearing, whilst maximising the association between the ingredient list with the output image. An 'ingredient' encoder is present to insert information into the deep learning model's inputs based on their feature representation.

Autoencoders are another distinct type of neural network which is essentially trained to reconstruct an input image [30-32], and in the process learns feature representations that can be used for different downstream tasks. Given an input, an autoencoder typically encodes this input into a compressed representation (i.e., a bottleneck layer, which is sometimes implemented via sparsity constraints). The knowledge represented in this bottleneck may reveal useful patterns or correlations between input variables. In the subsequent portion of the network, the compressed representation is decoded back into a state that is as similar to the input as possible. The decoding aspect of autoencoders is an important component of our chosen solution.

In 2016, Van Den Oord et al. [33] reported the possibility of generating new images from a data set conditional on their class (Conditional Image Generation) via PixelCNN Decoders. This specific model would be capable of operating on any vector, descriptive labels, or tags. A Pixel CNN Decoder is essentially an autoregressive model whereby the model maps the surrounding pixels in order to predict the next pixel sequentially. This can lead to improvements in the quality of the images generated. However, the presence of blind spot(s) in the receptive field of the Pixel CNN can affect the prediction of the model. In order to alleviate this problem, two stacks of CNN's are used. The images generated by the Conditional PixelCNN tend to be diverse and realistic based on the conditional category used.

Research on improving the current PixelCNN model was reported in 2017 by Salimans et al. [34]. Salimans et al. [34] introduced a new model named PixelCNN++ with the following changes: a) instead of applying a 256-way softmax, PixelCNN++ applies a discretized logistic mixture likelihood on the pixels of an image, b) downsampling was used to capture the image structure at different resolutions, c) analysing the condition on the whole image pixels, compared to RGH sub-pixels, d) introducing short-cut connections to speed up the optimization process. e) regularising the deep learning model using dropout. Apart from computational and memory costs, one of the key shortcomings of Traditional PixelCNN models is that PixelCNN has a slow learning process.

Out of the multiple feasible generative models that could have been adopted, we chose a simple approach, since this simplicity would help with memory efficiency, interpretability and ease of training. This approach was proposed by Al Rahhal et al. (2019) [35] and aims to convert 1-D Electrocardiogram (ECG) signals into 2-D images, which is broadly consistent with our problem setup. In [35], these 2-D images would then be used to perform classification of the diagrams based on 4 different labels which are N (Normal), S (Supraventricular), V (Ventricular) and F (Fusion) respectively. Al Rahhal et al.'s model contained both a generative and discriminative module. The generative module aims to generate an image while the discriminative module aims to perform the classification. However, as the aim of

our project is solely to generate an image based on a set of finite variables, some modifications have been made to the original model which will be further described in the research methodology section.

2. Research Methodology

2.1. Experimental design

Pavement bricks were cored to incorporate with PCMs are shown in Fig. 1. The pavement brick holes were filled with paraffin wax (PW), stearic acids (SA) and lauric acids (LA) with different formulations. The physical properties of the PCMs are shown in Table 1. The experiments were conducted at Cheras, Selangor, Malaysia. Samples were placed under the sun along with the respective control samples without PCM. The temperature profile of each sample was recorded at different time. A thermal imager (Testo 865, Germany) was used to capture the thermography of the samples and the temperature profiles were obtained through the testo IRSOFT Software, version 4.7. All experimental data collected are shown in Appendix A, Tables A-1 to A-68.



Fig. 1. Pavement bricks with phase change materials (PCMs)

Table 1. Properties and type of phase change materials (PCMs) used in this study*.

PCM	Molecular weight g/mol	Melting point, °C	Flash point, °C	Vapour pressure	Relative density, g/cm ³
Lauric acid (C ₁₂ H ₂₄ O ₂)	200.32	44 - 46	160 - 165	67 hPa at 210 °C	0.883
Stearic acid (C ₁₈ H ₃₆ O ₂)	248.48	67 - 72	113	1 hPa at 173.7 °C	0.845
Paraffin Wax	341.44	58 - 60	113	N/A	0.88

*Data obtained from SDS provided by Chemiz (M) Sdn. Bhd.

2.2. Modelling

The present study used machine learning and deep learning approach to predict the temperature profile of bricks integrated with PCM.

2.2.1. Deep learning approach

Since the target problem fits the general pattern of mapping a 1D vector of physical variables into 2D heat maps, the work of Al Rahhal et al. [35] was chosen as a basis for customisation. The solution proposed by Al Rahhal et al. [35] consisted of both generative and discriminatory modules. The aim of the generative module was to convert 1D Electrocardiogram (ECG) signals into 2D images, whereas the discriminatory component, involved taking these 2D images and classifying them into 4 different labels, i.e.: N (Normal), S (Supraventricular), V (Ventricular) and F (Fusion). Since our goal was to generate heat maps from a set of physical variables, this study focused on adapting the generative component of Al Rahhal et al.'s model. [35].

Figure 2 provides a high-level depiction of the proposed model and illustrates some of the key adaptations employed relative to the model of Al Rahhal et al. [35]. The input to the first fully connected layer was modified to match the number of input variables, which was 11. In the original model, each convolutional block contained the following sequence of operations: upsampling, convolution, batchnorm, leakyReLU, and dropout. Upsampling within our model was removed since we reshaped the output from the second fully connected layer to match with the original image's dimension at the reshaping layer. This reshaping layer was responsible for converting the initial 1D representation into a 2D representation. After preliminary experimentation, it was found that batchnorm and dropout were not helpful for our specific domain, and therefore they were removed. Finally, the number of core convolutional layers was increased to 3, with the last layer consisting of only convolution and no ReLU activation function. The ReLU activation function was also used in the first fully connected layer, whereas the second fully connected layer did not use any activation function.

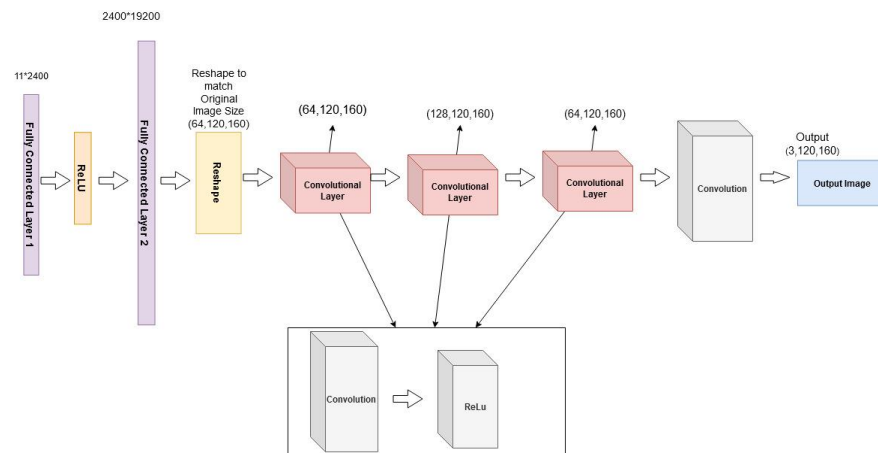


Fig. 2. High-level depiction of the model.

2.2.2. Model development

The model was developed using the Python language, the Anaconda distribution, which aims to facilitate package management for scientific computation (e.g. data science), and PyTorch as the key deep learning framework. The model was trained

on a laptop with an Intel Core i7-8750H Processor (4x 2.20GHz), an Nvidia Geforce GTX 1050 TI graphics card, and 8 GBs of RAM. Versioning was controlled via git and GitHub, and as such, the code for the model can be found here: <https://github.com/Shanahan-Suresh/segp-group4a-deep-learning-network>.

2.2.3. Data summary

The raw data resulting from the physical experiments is depicted in Appendix A composed of the following variables: Temperature (°C), Humidity (%), Wind speed (km/hr), Aluminium Temperature (°C), Chemical Temperature (°C), Lauric Acid (presence), Stearic Acid (presence), Paraffin Wax (presence), Paraffin Wax Composition (g), Lauric Acid Composition (g), and Stearic Acid Composition (g).

To represent the data in a convenient format for the neural network, the data was converted into a data frame format, each variable corresponding to a column in the data frame. The values were then normalized between 0 and 1, using the lowest and highest value for each corresponding column (with the exception of 'presence' variables, as 0 and 1 simply denote the absence or presence of those chemicals in the brick composition). Finally, all empty cells within the data frame were set to a default value of 0.

The normalized data was then split into a training set and a test set with a ratio of 9:1. Additionally, for the purpose of training the neural network, the original heatmap images were resized to a dimension of 160 x 120 pixels.

2.2.4. Hyper-parameter settings

After several preliminary experiments and several rounds of hyperparameter tuning, it was found that stochastic gradient descent (SGD) as the optimizer, and a learning rate and momentum of 0.009 and 0.9 respectively, worked best for our problem.

3. Results and Discussion

3.1. Temperature difference in control samples

A slight temperature difference can be seen in pavement bricks with and without PCMs. This difference can be as high as 0.12°C in terms of average pavement surface temperature and 0.10°C in terms of average pavement temperature. For pavement bricks with PCMs, some sections on the top surface area were replaced with PCMs with different formulations. It was found that the solar irradiance has a unit of watt per meter square, therefore, the greater the surface area exposed to the solar radiation, the higher the solar heat energy that is absorbed by the brick.

3.2. Impacts of PCMs quantity on pavement temperature profiles

A non-linear relationship, which was almost linear, between the average pavement surface temperature and PCM quantity was obtained. As the PCM quantity increases, the average pavement surface temperature is decreasing with increasing gradient. This is due to the top of the PCM approaching the surface of the pavement, which leads to greater heat energy being absorbed in the near-surface region of the pavement. While the relationship of average pavement temperature and PCM quantity exhibits a non-perfect linear relationship, for the type of PCMs, the heat

gain reduction is almost identical with the same brick configuration, showing that LA melted up to 50% while PW was around 40%. However, regarding the total heat accumulated in PCM, it can be observed that the difference between the heat absorbed by LA and PW is not significant. In other words, under the weather conditions set for this simulation, the properties of LA and PW do not have drastic impacts on the temperature profiles while contact surface area plays a larger role. Further to this, it is worth noting that the greater thermal conductivity, the lower the average surface temperature [1].

3.3. Model prediction accuracy.

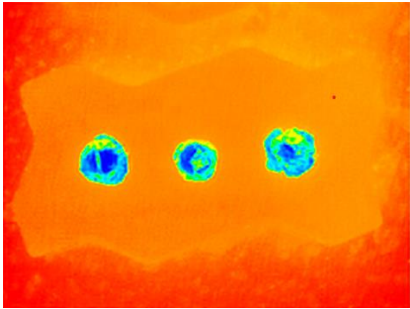
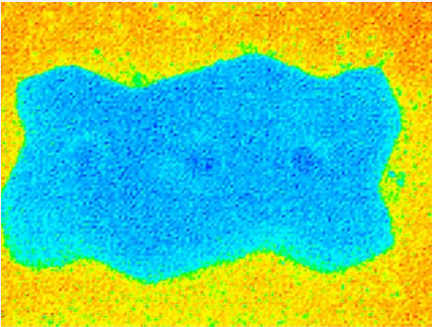
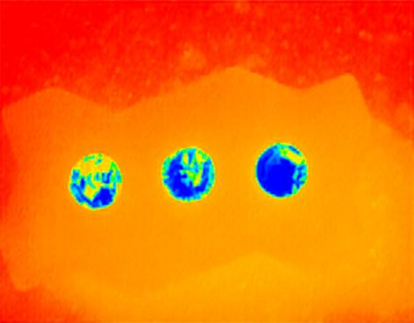
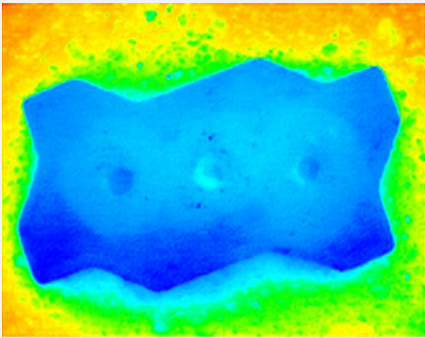
Regarding our modelling proof-of-concept, the results demonstrate that it is indeed feasible to develop simple models to effectively predict complex heat maps from a small set of relevant physical variables. Tables 2 and 3 illustrate the viability of the chosen modelling approach. The heat maps in Table 2 represent real heat maps in the test set, corresponding to sets of physical variables, whereas the images in Table 3 depict the corresponding heat maps generated by the model, given the same sets of physical variables. To evaluate the model quantitatively, the mean squared error between heat maps from the test set and corresponding predictions was computed, yielding a value of 0.0465, which, despite allowing space for improvement, is again consistent with the viability of the approach.

Mean Squared Error (MSE) was selected as the preferred evaluation metric for the developed deep learning model due to its characteristic of squaring the absolute distance between predicted and expected values. The squaring of distances leads to this metric punishing larger errors compared to the Mean Absolute Error (MAE) metric that only averages the absolute differences between predicted and expected values. This form of evaluation is better at capturing the impact of outliers on the deep learning model's expected prediction. As MSE is a negatively oriented score, the lower the MSE the better the model at handling outliers.

Apart from the promising quantitative test error mentioned above, we can also make the following qualitative observations. Successful predictions involve not only the highly localized temperature changes involving the specific PCA formulations, but also involve the surrounding general areas too. These surrounding areas, being larger and relatively more complex in shape, and potentially subject to additional variables not captured by the dataset, potentially contribute more to the error. However, in spite of these additional complexities, the figure shows that the model is still capable of capturing the general shape and relative temperature profiles of the actual heat maps.

Figure 3 provides an example depiction of the training process. The graph shows that the training procedure is relatively stable with the training error decreasing consistently and without significant oscillations. It can be seen that even at epoch 300 the model is still improving the training error which shows that the model is very capable of fitting the data. Moreover, the validation curve shows that the model is not overfitting excessively, which means that the model is capable of discovering valid underlying associations between the physical variables and corresponding heat maps and is thus capable of effectively generalizing to new instances.

Table 2. Example test images.

Test image ID	Test heat map images
1	
2	
3	
4	

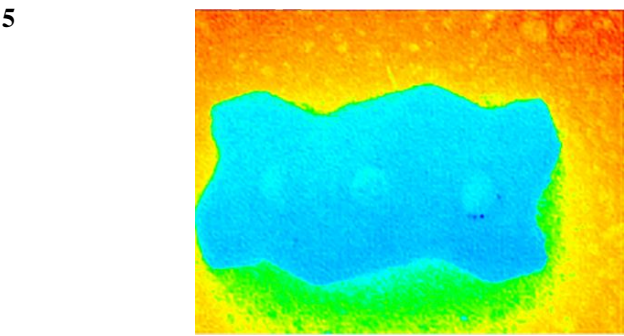
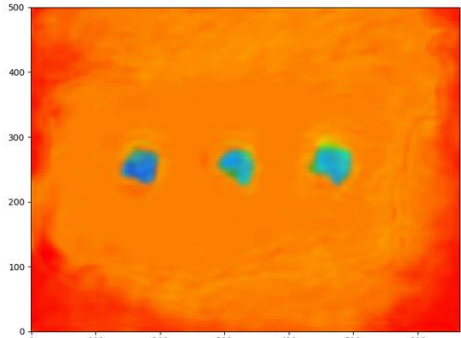
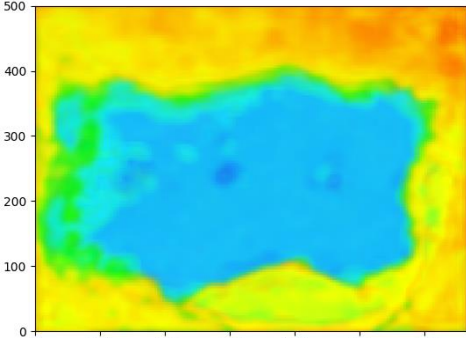
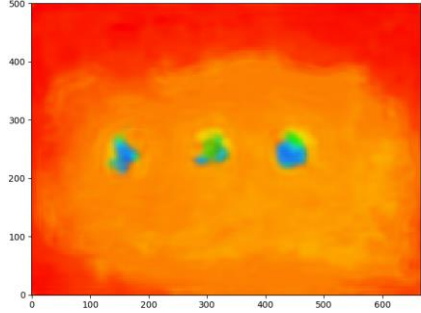


Table 3. Generated heat map images.

Test image ID	Predicted heat map images
1	
2	
3	

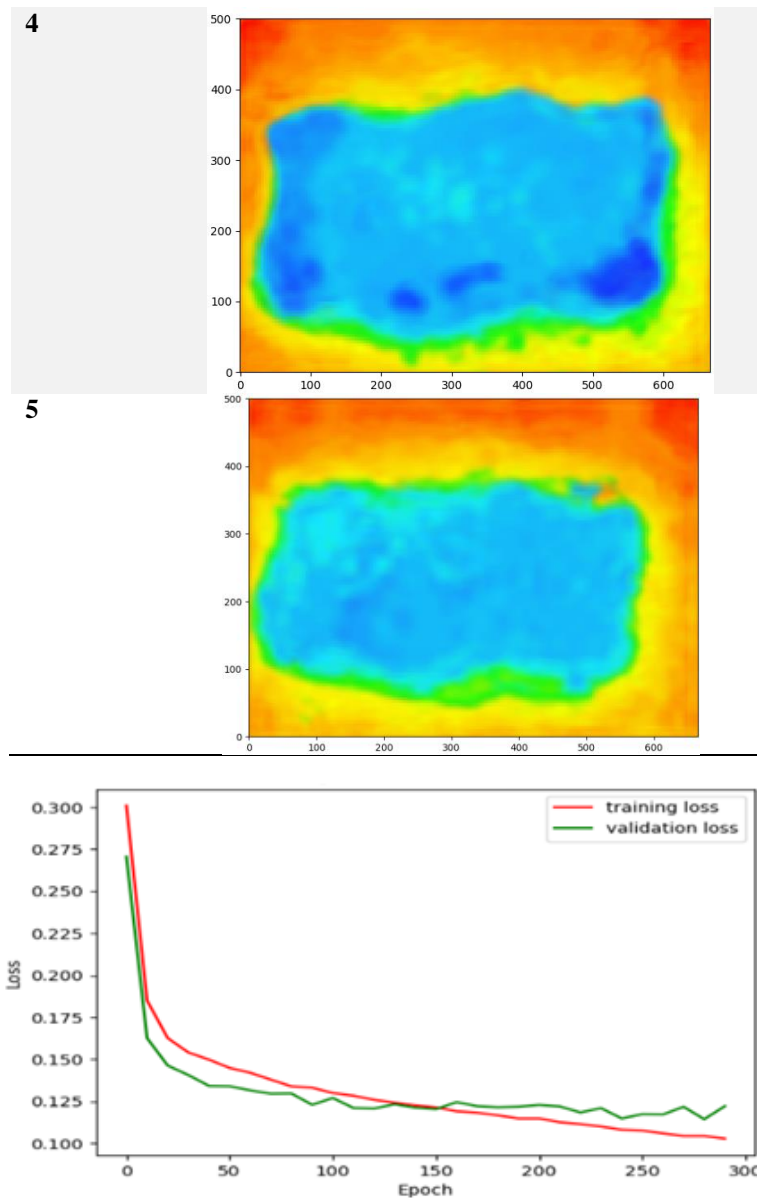


Fig. 3. Training and validation loss graph.

4. Conclusions

A machine learning solution was designed to evaluate the temperature profile of PCM incorporated into pavement bricks. In this study, the deep learning model developed was able to predict the surface temperature profiles of the pavement bricks with a mean squared error of 0.0465. The model was shown to be capable of generalizing to a variety of temperature profiles and PCM formulations. To the best of our knowledge this is the first time that such a dataset has been created, and deep learning models have been developed for the purpose of predicting heat maps from PCM related

variables. As such, this work provides an initial step towards helping future authors benchmark relevant models. Although the model we developed, which is an adaptation of Al Rahhal et al.'s model [35], was effective at predicting heat maps, we believe that future work will involve extending the dataset further and developing new and improved types of generative models for heat map generation. Once this happens, it will be possible to conduct an extensive and systematic benchmark comparison, which will usher a new age of efficient and scalable experimentation in the design of pavement bricks incorporated with phase change materials (PCMs).

Abbreviations

ECG	Electrocardiogram
F	Fusion
LA	Lauric acids
N	Normal
O	Organic Material
PCM	Phase Change Materials
PW	Paraffin wax
S	Supraventricular
SA	Stearic acids
SGD	Stochastic gradient descent
UHI	Urban Heat Island
V	Ventricular

References

1. Rizwan, A.M.; Dennis, L.Y.C.; and Liu, C. (2008). A review on the generation, determination and mitigation of Urban Heat Island. *Journal of Environmental Sciences*, 20(1), 120-128.
2. Hajat, S.; Vardoulakis, S.; Heaviside, C.; and Eggen, B. (2014). Climate change effects on human health: Projections of temperature-related mortality for the UK during the 2020s, 2050s and 2080s. *Journal of Epidemiology and Community Health*, 68(7), 641-648.
3. Wong, L.P.; Alias, H.; Aghamohammadi, N.; Aghazadeh, S.; and Nik Sulaiman, N.M. (2017). Urban heat island experience, control measures and health impact: A survey among working community in the city of Kuala Lumpur. *Sustainable Cities and Society*, 35, 660-668.
4. Al-Yasiri, Q.; and Szabó, M. (2020). Incorporation of phase change materials into building envelope for thermal comfort and energy saving: A comprehensive analysis. *Journal of Building Engineering*, 102122.
5. Djekic, J.; Djukic, A.; Vukmirovic, M.; Djekic, P.; and Brankovic, M. D. (2018). Thermal comfort of pedestrian spaces and the influence of pavement materials on warming up during summer. *Energy and buildings*, 159, 474-485.
6. Manteghi, G.; Mostofa, T.; Yahaya, A.S.; and Lamit, H.B. (2020). Thermal comfort consequence of pavement material at pedestrian level in Melaka Town. *Proceedings of International Conference on Architecture and Civil Engineering (ICACE) 2019*, Springer, Singapore, 1-8.
7. Taleghani, M.; and Berardi, U. (2018). The effect of pavement characteristics on pedestrians' thermal comfort in Toronto. *Urban climate*, 24, 449-459.

8. Saxena, R.; Rakshit, D.; and Kaushik, S.C. (2020). Experimental assessment of Phase Change Material (PCM) embedded bricks for passive conditioning in buildings. *Renewable Energy*, 149, 587-599.
9. Alawadhi, E.M. (2008). Thermal analysis of a building brick containing phase change material. *Energy and Buildings*, 40(3), 351-357.
10. Arunkumar, D.; Ramu, M.; Murugan, R.; Kannan, S.; Arun, S.; and Baskar, S. (2020). Investigation of heat transfer of wall with and without using phase change material. *Materials Today: Proceedings*, 33, 2646-2650.
11. Kumar, S.; Arun Prakash, S.; Pandiyarajan, V.; Geetha, N. B.; Antony Aroul Raj, V.; and Velraj, R. (2020). Effect of phase change material integration in clay hollow brick composite in building envelope for thermal management of energy efficient buildings. *Journal of Building Physics*, 43(4), 351-364.
12. Aketouane, Z.; Malha, M.; Bruneau, D.; Bah, A.; Michel, B.; Asbik, M.; and Ansari, O. (2018). Energy savings potential by integrating Phase Change Material into hollow bricks: The case of Moroccan buildings. *Building Simulation*, 11(6), 1109-1122.
13. Athukorallage, B.; Dissanayaka, T.; Senadheera, S.; and James, D. (2018). Performance analysis of incorporating phase change materials in asphalt concrete pavements. *Construction and Building Materials*, 164, 419-432.
14. Refaa, Z.; Kakar, M.R.; Stamatiou, A.; Worlitschek, J.; Partl, M.N.; and Bueno, M. (2018). Numerical study on the effect of phase change materials on heat transfer in asphalt concrete. *International Journal of Thermal Sciences*, 133, 140-150.
15. Dehdezi, P.K.; Hall, M.R.; Dawson, A.R.; and Casey, S.P. (2013). Thermal, mechanical and microstructural analysis of concrete containing microencapsulated phase change materials. *International Journal of Pavement Engineering*, 14(5), 449-462.
16. Haurie, L.; Serrano, S.; Bosch, M.; Fernandez, A.I.; and Cabeza, L.F. (2016). Single layer mortars with microencapsulated PCM: Study of physical and thermal properties, and fire behaviour. *Energy and Buildings*, 111, 393-400.
17. Du, Y.; Liu, P.; Wang, J.; Wang, H.; Hu, S.; Tian, J.; and Li, Y. (2019). Laboratory investigation of phase change effect of polyethylene glycol on asphalt binder and mixture performance. *Construction and Building Materials*, 212, 1-9.
18. Vakhshouri, A.R. (2019). Paraffin as phase change material. In (Ed.), *Paraffin -An Overview*. IntechOpen [Online]. Available: <https://www.intechopen.com/chapters/70480>.
19. Keleş, S.; Kaygusuz, K.; and Sari, A. (2005). Lauric and myristic acids eutectic mixture as phase change material for low-temperature heating applications. *International Journal of Energy Research*, 29, 857-870.
20. Sari A.; and Kaygusuz K. (2002). Thermal performance of a eutectic mixture of lauric and stearic acids as PCM encapsulated in the annulus of two concentric pipes. *Solar Energy*, 72, 493-504.
21. Lu, Y.; Chen, D.; Olaniyi, E.; and Huang, Y. (2022). Generative adversarial networks (GANs) for image augmentation in agriculture: A systematic review. *Computers and Electronics in Agriculture*, 200, 107208.

22. Singh, N.K.; and Raza, K. (2021). Medical image generation using generative adversarial networks: A review. *Health informatics: A computational perspective in healthcare*, 77-96.
23. Chen, Y.; Yang, X.H.; Wei, Z.; Heidari, A.A.; Zheng, N.; Li, Z.; Chen, H.; Hu, H.; Zhou, Q.; and Guan, Q. (2022). Generative adversarial networks in medical image augmentation: a review. *Computers in Biology and Medicine*, 144, 105382.
24. Park, S.W.; Ko, J.S.; Huh, J.H.; and Kim, J.C. (2021). Review on generative adversarial networks: focusing on computer vision and its applications. *Electronics*, 10(10), 1216.
25. Yang, Y.; Liu, F.; Yao, J.; Iglauer, S.; Sajjadi, M.; Zhang, K.; Sun, H.; Zhang, L.; Zhong, J.; and Lisitsa, V. (2022). Multi-scale reconstruction of porous media from low-resolution core images using conditional generative adversarial networks. *Journal of Natural Gas Science and Engineering*, 99, 104411.
26. Abu-Srhan, A.; Abushariah, M.A.; and Al-Kadi, O.S. (2022). The effect of loss function on conditional generative adversarial networks. *Journal of King Saud University-Computer and Information Sciences*, 34, 6977-6988.
27. Hettiarachchi, P.; Nawaratne, R.; Alahakoon, D.; De Silva, D.; and Chilamkurti, N. (2021). Rain streak removal for single images using conditional generative adversarial networks. *Applied Sciences*, 11(5), 2214.
28. Mishra, P.; and Herrmann, I. (2021). GAN meets chemometrics: Segmenting spectral images with pixel2pixel image translation with conditional generative adversarial networks. *Chemometrics and Intelligent Laboratory Systems*, 215, 104362.
29. Han, F., Guerrero, R. and Pavlovic, V. (2020). Cookgan: Meal image synthesis from ingredients. *Proceedings of the IEEE/CVF Winter Conference on Applications of Computer Vision*, 1450-1458.
30. He, K.; Chen, X.; Xie, S.; Li, Y.; Dollár, P.; and Girshick, R. (2022). Masked autoencoders are scalable vision learners. *Proceedings of the IEEE/CVF Conference on Computer Vision and Pattern Recognition*, 16000-16009.
31. Baur, C.; Denner, S.; Wiestler, B.; Navab, N.; and Albarqouni, S. (2021). Autoencoders for unsupervised anomaly segmentation in brain MR images: a comparative study. *Medical Image Analysis*, 69, 101952.
32. Wu, Y.; Li, J.; Yuan, Y.; Qin, A.K.; Miao, Q.G.; and Gong, M.G. (2021). Commonality autoencoder: Learning common features for change detection from heterogeneous images. *IEEE Transactions on Neural Networks and Learning Systems*, 33(9), 4257-4270.
33. Van den Oord, A.; Kalchbrenner, N.; Espeholt, L.; Vinyals, O. and Graves, A. (2016). Conditional image generation with pixelcnn decoders. *Advances in neural information processing systems*, 29. *Proceedings of NIPS'16: Proceedings of the 30th International Conference on Neural Information Processing Systems*, 4797-4805.
34. Salimans, T.; Karpathy, A.; Chen, X.; and Kingma, D.P. (2017). Pixelcnn++: Improving the pixelcnn with discretized logistic mixture likelihood and other modifications. *arXiv preprint arXiv:1701.05517*.
35. Al Rahhal, M.M.; Bazi, Y.; Almubarak, H.; Alajlan, N.; and Al Zuair, M. (2019). Dense convolutional networks with focal loss and image generation for electrocardiogram classification. *IEEE Access*, 7, 182225-182237.

Appendix A

Experimental data

Table. A-1. Experimental data and SR files code.

Parameters	Temperature, °C	Humidity, %	Wind speed, km/h
	27	81	3
Chemicals	Composition, g	SR file number	Aluminium temperature
Lauric acid	3	558	26.5
Lauric acid	3	559	24.8
Stearic acid	3	560	26.4
Stearic acid	3	561	26.3
Paraffin wax	3	562	26.2
Paraffin wax	3	563	25.9
Control	Nil	564	25.6
Control	Nil	565	25.4

Table. A-2. Experimental data and SR files code.

Parameters	Temperature, °C	Humidity, %	Wind speed, km/h
	29	74	3
Chemicals	Composition, g	SR file number	Aluminium temperature
Lauric acid	3	580	28.6
Lauric acid	3	581	26.6
Stearic acid	3	582	28.6
Stearic acid	3	583	30
Paraffin wax	3	584	26.7
Paraffin wax	3	585	29.3
Control	Nil	586	29.3
Control	Nil	587	29.4

Table. A-3. Experimental data and SR files code.

Parameters	Temperature, °C	Humidity, %	Wind speed, km/h
	29	71	5
Chemicals	Composition, g	SR file number	Aluminium temperature
Lauric acid	3	601	34
Lauric acid	3	602	35.8
Stearic acid	3	603	31.4
Stearic acid	3	604	34.8
Paraffin wax	3	605	36.7
Paraffin wax	3	606	35.2
Control	Nil	607	32.4
Control	Nil	608	33.7

Table. A-4. Experimental data and SR files code.

Parameters	Temperature, °C	Humidity, %	Wind speed, km/h
	31	67	11
Chemicals	Composition, g	SR file number	Aluminium temperature
Lauric acid	3	621	40.6
Lauric acid	3	622	37.5
Stearic acid	3	623	36.7
Stearic acid	3	624	36.5
Paraffin wax	3	625	40.6
Paraffin wax	3	626	38.2
Control	Nil	627	37
Control	Nil	628	36

Table. A-5. Experimental data and SR files code.

Parameters	Temperature, °C	Humidity, %	Wind speed, km/h
	31	65	16
Chemicals	Composition, g	SR file number	Aluminium temperature
Lauric acid	3	641	42.2
Lauric acid	3	642	46.8
Stearic acid	3	643	42.8
Stearic acid	3	644	40
Paraffin wax	3	645	40.5
Paraffin wax	3	646	39.4
Control	Nil	647	43.7
Control	Nil	648	44.7

Table. A-6. Experimental data and SR files code.

Parameters	Temperature, °C	Humidity, %	Wind speed, km/h
	32	63	16
Chemicals	Composition, g	SR file number	Aluminium temperature
Lauric acid	3	661	40.9
Lauric acid	3	662	38.6
Stearic acid	3	663	38.2
Stearic acid	3	664	40.7
Paraffin wax	3	665	37.5
Paraffin wax	3	666	35.9
Control	Nil	667	38
Control	Nil	668	39.1

Table. A-7. Experimental data and SR files code.

Parameters	Temperature, °C	Humidity, %	Wind speed, km/h
	32	60	18
Chemicals	Composition, g	SR file number	Aluminium temperature
Lauric acid	3	681	40.9
Lauric acid	3	682	38.6
Stearic acid	3	683	38.2
Stearic acid	3	684	40.7
Paraffin wax	3	685	37.5
Paraffin wax	3	686	35.9
Control	Nil	687	38
Control	Nil	688	39.1

Table. A-8. Experimental data and SR files code.

Parameters	Temperature, °C	Humidity, %	Wind speed, km/h
	28	77	8
Chemicals	Composition, g	SR file number	Aluminium temperature
Lauric acid	3	273	32.4
Lauric acid	3	274	32.3
Stearic acid	3	275	31.8
Stearic acid	3	276	31.9
Paraffin wax	3	277	30
Paraffin wax	3	278	31.1

Table. A-9. Experimental data and SR files code.

Parameters	Temperature, °C	Humidity, %	Wind speed, km/h
	29	75	8
Chemicals	Composition, g	SR file number	Chemical temperature
Lauric acid	3	280	38.5
Lauric acid	3	281	39.8
Stearic acid	3	282	38.5
Stearic acid	3	283	38.5
Paraffin wax	3	284	37.3
Paraffin wax	3	285	39.1

Table. A-10. Experimental data and SR files code.

Parameters	Temperature, °C	Humidity, %	Wind speed, km/h
	31	70	15
Chemicals	Composition, g	SR file number	Chemical temperature
Lauric acid	3	292	40.7
Lauric acid	3	293	41
Stearic acid	3	294	40.6
Stearic acid	3	295	39.6
Paraffin wax	3	296	39.1
Paraffin wax	3	297	40.8

Table. A-11. Experimental data and SR files code.

Parameters	Temperature, °C	Humidity, %	Wind speed, km/h
	29	79	9
Chemicals	Composition, g	SR file number	Chemical temperature
Lauric acid	3	307	38.9
Lauric acid	3	308	39.3
Stearic acid	3	309	38.7
Stearic acid	3	310	38.2
Paraffin wax	3	311	37.5
Paraffin wax	3	312	38.2

Table. A-12. Experimental data and SR files code.

Parameters	Temperature, °C	Humidity, %	Wind speed, km/h
	26	87	3
Chemicals	Composition, g	SR file number	Chemical temperature
Lauric acid	3	324	26.9
Lauric acid	3	325	26.6
Stearic acid	3	326	26.6
Stearic acid	3	327	26.3
Paraffin wax	3	328	26.3
Paraffin wax	3	329	26.3

Table. A-13. Experimental data and SR files code.

Parameters	Temperature, °C	Humidity, %	Wind speed, km/h
	28	77	8
Chemicals	Composition, g	SR file number	Chemical temperature
Lauric acid	3	378	37.2
Lauric acid	3	379	37.4
Stearic acid	3	380	36.7
Stearic acid	3	381	36.1
Paraffin wax	3	382	33.8
Paraffin wax	3	383	34.4
Control	Nil	384	36.1
Control	Nil	385	36.4

Table. A-14. Experimental data and SR files code.

Parameters	Temperature, °C	Humidity, %	Wind speed, km/h
	29	75	8
Chemicals	Composition, g	SR file number	Chemical temperature
Lauric acid	3	407	42.4
Lauric acid	3	408	44.2
Stearic acid	3	409	43.2
Stearic acid	3	410	43
Paraffin wax	3	411	41.4
Paraffin wax	3	412	42.1
Control	Nil	413	41.9
Control	Nil	414	41.4

Table. A-15. Experimental data and SR files code.

Parameters	Temperature, °C	Humidity, %	Wind speed, km/h
	30	72	10
Chemicals	Composition, g	SR file number	Chemical temperature
Lauric acid	3	466	41.3
Lauric acid	3	467	41.6
Stearic acid	3	468	41.5
Stearic acid	3	469	41.4
Paraffin wax	3	470	41
Paraffin wax	3	471	40.7
Control	Nil	474	40.8
Control	Nil	475	40.6

Table. A-16. Experimental data and SR files code.

Parameters	Temperature, °C	Humidity, %	Wind speed, km/h
	27	89	7
Chemicals	Composition, g	SR file number	Chemical temperature
Lauric acid	3	499	42.2
Lauric acid	3	500	42.5
Stearic acid	3	501	42.7
Stearic acid	3	502	42.7
Paraffin wax	3	503	42.6
Paraffin wax	3	504	42.1
Control	Nil	505	42.3

Table. A-17. Experimental data and SR files code.

Parameters	Temperature, °C	Humidity, %	Wind speed, km/h
	25	89	3
Chemicals	Composition, g	SR file number	Chemical temperature
Lauric acid	3	882	24.8
Stearic acid	3	883	25.2
Paraffin wax	3	884	25.5
Lauric acid	2	885	25.9
Stearic acid	2		
Control	Nil	886	25.9

Table. A-18. Experimental data and SR files code.

Parameters	Temperature, °C	Humidity, %	Wind speed, km/h
	26	84	2
Chemicals	Composition, g	SR file number	Chemical temperature
Lauric acid	3	887	31.7
Stearic acid	3	888	32.1
Paraffin wax	3	889	31.7
Lauric acid	2	890	31.9
Stearic acid	2		
Control	2	891	32.2

Table. A-19. Experimental data and SR files code.

Parameters	Temperature, °C	Humidity, %	Wind speed, km/h
	27	82	3
Chemicals	Composition, g	SR file number	Chemical temperature
Lauric acid	3	892	35.6
Stearic acid	3	893	35.7
Paraffin wax	3	894	34.7
Lauric acid	2	895	35.8
Stearic acid	2		
Control	2	896	35.9

Table. A-20. Experimental data and SR files code.

Parameters	Temperature, °C	Humidity, %	Wind speed, km/h
	28	77	3
Chemicals	Composition, g	SR file number	Chemical temperature
Lauric acid	3	897	39.4
Stearic acid	3	898	39.8
Paraffin wax	3	899	35.5
Lauric acid	2	900	44.1
Stearic acid	2		
Control	2	901	34.3

Table. A-21. Experimental data and SR files code.

Parameters	Temperature, °C	Humidity, %	Wind speed, km/h
	28	74	5
Chemicals	Composition, g	SR file number	Chemical temperature
Lauric acid	3	902	46.5
Stearic acid	3	903	47.4
Paraffin wax	3	904	42.1
Lauric acid	2	905	50.1
Stearic acid	2		
Control	2	906	42.1

Table. A-22. Experimental data and SR files code.

Parameters	Temperature, °C	Humidity, %	Wind speed, km/h
	29	72	6
Chemicals	Composition, g	SR file number	Chemical temperature
Lauric acid	3	907	48
Stearic acid	3	908	49.2
Paraffin wax	3	909	43
Lauric acid	2	910	51.3
Stearic acid	2		
Control	2	911	42.4

Table. A-23. Experimental data and SR files code.

Parameters	Temperature, °C	Humidity, %	Wind speed, km/h
	30	69	8
Chemicals	Composition, g	SR file number	Chemical temperature
Lauric acid	3	912	45.1
Stearic acid	3	913	45.9
Paraffin wax	3	914	41
Lauric acid	2	915	47.5
Stearic acid	2		
Control	2	916	41.6

Table. A-24. Experimental data and SR files code.

Parameters	Temperature, °C	Humidity, %	Wind speed, km/h
	30	67	8
Chemicals	Composition, g	SR file number	Chemical temperature
Lauric acid	3	917	48.8
Stearic acid	3	918	52.5
Paraffin wax	3	919	46.1
Lauric acid	2	920	53.5
Stearic acid	2		
Control	2	921	46.9

Table. A-25. Experimental data and SR files code.

Parameters	Temperature, °C	Humidity, %	Wind speed, km/h
	31	66	8
Chemicals	Composition, g	SR file number	Chemical temperature
Lauric acid	3	922	46.1
Stearic acid	3	923	46.2
Paraffin wax	3	924	43
Lauric acid	2	925	47.9
Stearic acid	2		
Control	2	926	43.8

Table. A-26. Experimental data and SR files code.

Parameters	Temperature, °C	Humidity, %	Wind speed, km/h
	31	66	8
Chemicals	Composition, g	SR file number	Chemical temperature
Lauric acid	3	927	48.9
Stearic acid	3	928	49.6
Paraffin wax	3	929	48.9
Lauric acid	2	930	50
Stearic acid	2		
Control	2	931	50.3

Table. A-27. Experimental data and SR files code.

Parameters	Temperature, °C	Humidity, %	Wind speed, km/h
	31	63	8
Chemicals	Composition, g	SR file number	Chemical temperature
Lauric acid	3	932	45.8
Stearic acid	3	933	46.8
Paraffin wax	3	934	46.9
Lauric acid	2	935	47.3
Stearic acid	2		
Control	2	936	47.6

Table. A-28. Experimental data and SR files code.

Parameters	Temperature, °C	Humidity, %	Wind speed, km/h
	31	62	10
Chemicals	Composition, g	SR file number	Chemical temperature
Lauric acid	3	942	50.8
Stearic acid	3	943	52.7
Paraffin wax	3	944	49.1
Lauric acid	2		
Stearic acid	2	945	53.8
Control	Nil.	946	51.7

Table. A-29. Experimental data and SR files code.

Parameters	Temperature, °C	Humidity, %	Wind speed, km/h
	32	59	10
Chemicals	Composition, g	SR file number	Chemical temperature
Lauric acid	3	947	53.5
Stearic acid	3	948	53.8
Paraffin wax	3	949	52
Lauric acid	2	950	54
Stearic acid	2		
Control	Nil.	951	51.7

Table. A-30. Experimental data and SR files code.

Parameters	Temperature, °C	Humidity, %	Wind speed, km/h
	31	61	10
Chemicals	Composition, g	SR file number	Chemical temperature
Lauric acid	3	952	50.1
Stearic acid	3	954	50.9
Paraffin wax	3	955	50.3
Lauric acid	2	956	50.4
Stearic acid	2		
Control	Nil.	957	50.2

Table. A-31. Experimental data and SR files code.

Parameters	Temperature, °C	Humidity, %	Wind speed, km/h
	31	61	6
Chemicals	Composition, g	SR file number	Chemical temperature
Lauric acid	3	958	47.2
Stearic acid	3	959	47.7
Paraffin wax	3	960	45.6
Lauric acid	2	961	47.5
Stearic acid	2		
Control	Nil.	962	45.3

Table. A-32. Experimental data and SR files code.

Parameters	Temperature, °C	Humidity, %	Wind speed, km/h
	24	87	2
Chemicals	Composition, g	SR file number	Chemical temperature
Lauric acid	3	968	26.1
Stearic acid	3	969	25.9
Paraffin wax	3	970	26.1
Lauric acid	2	971	26.5
Stearic acid	2		
Control	Nil.	972	26.6

Table. A-33. Experimental data and SR files code.

Parameters	Temperature, °C	Humidity, %	Wind speed, km/h
	26	82	2
Chemicals	Composition, g	SR file number	Chemical temperature
Lauric acid	3	973	28.1
Stearic acid	3	974	28.3
Paraffin wax	3	975	28.6
Lauric acid	2	976	28.7
Stearic acid	2		
Control	Nil.	977	31.6

Table. A-34. Experimental data and SR files code.

Parameters	Temperature, °C	Humidity, %	Wind speed, km/h
	26	80	2
Chemicals	Composition, g	SR file number	Chemical temperature
Lauric acid	3	978	31.3
Stearic acid	3	979	31.9
Paraffin wax	3	980	32.2
Lauric acid	2	981	32.7
Stearic acid	2		
Control	Nil.	982	36.4

Table. A-35. Experimental data and SR files code.

Parameters	Temperature, °C	Humidity, %	Wind speed, km/h
	27	75	2
Chemicals	Composition, g	SR file number	Chemical temperature
Lauric acid	3	983	38.2
Stearic acid	3	984	38.2
Paraffin wax	3	986	37.9
Lauric acid	2	987	38.4
Stearic acid	2		
Control	Nil.	988	41.2

Table. A-36. Experimental data and SR files code.

Parameters	Temperature, °C	Humidity, %	Wind speed, km/h
	28	69	3
Chemicals	Composition, g	SR file number	Chemical temperature
Lauric acid	3	989	44
Stearic acid	3	990	43.6
Paraffin wax	3	991	43.2
Lauric acid	2	992	44.3
Stearic acid	2		
Control	Nil.	993	45.9

Table. A-37. Experimental data and SR files code.

Parameters	Temperature, °C	Humidity, %	Wind speed, km/h
	30	64	5
Chemicals	Composition, g	SR file number	Chemical temperature
Lauric acid	3	994	44.8
Stearic acid	3	995	44.8
Paraffin wax	3	996	45.3
Lauric acid	2	997	48.4
Stearic acid	2		
Control	Nil.	998	48.4

Table. A-38. Experimental data and SR files code.

Parameters	Temperature, °C	Humidity, %	Wind speed, km/h
	31	62	5
Chemicals	Composition, g	SR file number	Chemical temperature
Lauric acid	3	999	51.7
Stearic acid	3	1000	51.4
Paraffin wax	3	1001	51.3
Lauric acid	2	1002	54
Stearic acid	2		
Control	Nil.	1003	53.9

Table. A-39. Experimental data and SR files code.

Parameters	Temperature, °C	Humidity, %	Wind speed, km/h
	32	59	6
Chemicals	Composition, g	SR file number	Chemical temperature
Lauric acid	3	1004	55.1
Stearic acid	3	1005	54.8
Paraffin wax	3	1006	54.6
Lauric acid	2	1007	57.4
Stearic acid	2		
Control	Nil.	1008	57.6

Table. A-40. Experimental data and SR files code.

Parameters	Temperature, °C	Humidity, %	Wind speed, km/h
	32	57	6
Chemicals	Composition, g	SR file number	Chemical temperature
Lauric acid	3	1009	58.2
Stearic acid	3	1010	59
Paraffin wax	3	1011	56.3
Lauric acid	2	1012	59.7
Stearic acid	2		
Control	Nil.	1013	59.6

Table. A-41. Experimental data and SR files code.

Parameters	Temperature, °C	Humidity, %	Wind speed, km/h
	32	56	8
Chemicals	Composition, g	SR file number	Chemical temperature
Lauric acid	3	1014	60
Stearic acid	3	1015	59.5
Paraffin wax	3	1016	58.8
Lauric acid	2	1017	60.9
Stearic acid	2		
Control	Nil.	1018	56

Table. A-42. Experimental data and SR files code.

Parameters	Temperature, °C	Humidity, %	Wind speed, km/h
	32	56	8
Chemicals	Composition, g	SR file number	Chemical temperature
Lauric acid	3	1019	62.5
Stearic acid	3	1020	62.1
Paraffin wax	3	1021	60.4
Lauric acid	2	1022	64.6
Stearic acid	2		
Control	Nil.	1023	64.5

Table. A-43. Experimental data and SR files code.

Parameters	Temperature, °C	Humidity, %	Wind speed, km/h
	32	56	8
Chemicals	Composition, g	SR file number	Chemical temperature
Lauric acid	3	1024	63.2
Stearic acid	3	1025	61.8
Paraffin wax	3	1027	61.5
Lauric acid	2	1028	65.4
Stearic acid	2		
Control	Nil.	1029	62.3

Table. A-44. Experimental data and SR files code

Parameters	Temperature, °C	Humidity, %	Wind speed, km/h
	33	55	8
Chemicals	Composition, g	SR file number	Chemical temperature
Lauric acid	3	1030	60.9
Stearic acid	3	1031	58.8
Paraffin wax	3	1032	59.4
Lauric acid	2	1033	62.6
Stearic acid	2		
Control	Nil.	1034	62

Table. A-45. Experimental data and SR files code

Parameters	Temperature, °C	Humidity, %	Wind speed, km/h
	33	56	10
Chemicals	Composition, g	SR file number	Chemical temperature
Lauric acid	3	1035	61.1
Stearic acid	3	1036	60.9
Paraffin wax	3	1037	60.7
Lauric acid	2	1038	63.1
Stearic acid	2		
Control	Nil.	1039	60.9

Table. A-46. Experimental data and SR files code

Parameters	Temperature, °C	Humidity, %	Wind speed, km/h
	33	55	10
Chemicals	Composition, g	SR file number	Chemical temperature
Lauric acid	3	1040	55
Stearic acid	3	1041	55.3
Paraffin wax	3	1042	54.8
Lauric acid	2	1043	57.8
Stearic acid	2		
Control	Nil.	1044	55.8

Table. A-47. Experimental data and SR files code

Parameters	Temperature, °C	Humidity, %	Wind speed, km/h
	33	56	11
Chemicals	Composition, g	SR file number	Chemical temperature
Lauric acid	3	1045	54.5
Stearic acid	3	1046	54.9
Paraffin wax	3	1047	55.2
Lauric acid	2	1048	58
Stearic acid	2		
Control	Nil.	1049	54.8

Table. A-48. Experimental data and SR files code

Parameters	Temperature, °C	Humidity, %	Wind speed, km/h
	32	58	10
Chemicals	Composition, g	SR file number	Chemical temperature
Lauric acid	3	1050	53.2
Stearic acid	3	1051	53.4
Paraffin wax	3	1052	52.5
Lauric acid	2	1053	53.4
Stearic acid	2		
Control	Nil.	1054	52.1

Table. A-49. Experimental data and SR files code

Parameters	Temperature, °C	Humidity, %	Wind speed, km/h
	32	58	10
Chemicals	Composition, g	SR file number	Chemical temperature
Lauric acid	3	1055	51.8
Stearic acid	3	1056	51.9
Paraffin wax	3	1057	48.3
Lauric acid	2	1058	49.4
Stearic acid	2		
Control	Nil.	1059	51.9

Table. A-50. Experimental data and SR files code

Parameters	Temperature, °C	Humidity, %	Wind speed, km/h
	25	85	3
Chemicals	Composition, g	SR file number	Chemical temperature
Lauric acid	3	1060	24.4
Stearic acid	3	1061	28.3
Paraffin wax	3	1062	22.7
Lauric acid	2	1063	19.5
Stearic acid	2		
Control	Nil.	1064	19.5

Table. A-51. Experimental data and SR files code

Parameters	Temperature, °C	Humidity, %	Wind speed, km/h
	26	82	3
Chemicals	Composition, g	SR file number	Chemical temperature
Lauric acid	3	1066	28.6
Stearic acid	3	1067	24
Paraffin wax	3	1068	21
Lauric acid	2	1069	23.5
Stearic acid	2		
Control	Nil.	1070	29.2

Table. A-52. Experimental data and SR files code

Parameters	Temperature, °C	Humidity, %	Wind speed, km/h
	27	79	3
Chemicals	Composition, g	SR file number	Chemical temperature
Lauric acid	3	1071	31.4
Stearic acid	3	1072	27.2
Paraffin wax	3	1073	30.9
Lauric acid	2	1074	32.5
Stearic acid	2		
Control	Nil.	1075	32.5

Table. A-53. Experimental data and SR files code

Parameters	Temperature, °C	Humidity, %	Wind speed, km/h
	27	78	3
Chemicals	Composition, g	SR file number	Chemical temperature
Lauric acid	3	1076	29
Stearic acid	3	1077	25.2
Paraffin wax	3	1078	32.2
Lauric acid	2	1079	33
Stearic acid	2		
Control	Nil.	1080	32.8

Table. A-54. Experimental data and SR files code

Parameters	Temperature, °C	Humidity, %	Wind speed, km/h
	27	78	3
Chemicals	Composition, g	SR file number	Chemical temperature
Lauric acid	3	1081	33.6
Stearic acid	3	1082	27.4
Paraffin wax	3	1083	33.7
Lauric acid	2	1084	30.6
Stearic acid	2		
Control	Nil.	1085	31.3

Table. A-55. Experimental data and SR files code

Parameters	Temperature, °C	Humidity, %	Wind speed, km/h
	29	70	5
Chemicals	Composition, g	SR file number	Chemical temperature
Lauric acid	3	1086	31.2
Stearic acid	3	1087	31.5
Paraffin wax	3	1088	37.7
Lauric acid	2	1089	35
Stearic acid	2		
Control	Nil.	1090	36.8

Table. A-56. Experimental data and SR files code

Parameters	Temperature, °C	Humidity, %	Wind speed, km/h
	29	69	5
Chemicals	Composition, g	SR file number	Chemical temperature
Lauric acid	3	1091	35.7
Stearic acid	3	1092	21.4
Paraffin wax	3	1093	27.1
Lauric acid	2	1094	32.8
Stearic acid	2		
Control	Nil.	1095	32.3

Table. A-57. Experimental data and SR files code.

Parameters	Temperature, °C	Humidity, %	Wind speed, km/h
	29	68	5
Chemicals	Composition, g	SR file number	Chemical temperature
Lauric acid	3	1096	35.1
Stearic acid	3	1097	27.1
Paraffin wax	3	1098	37.5
Lauric acid	2	1099	42.2
Stearic acid	2		
Control	Nil.	1100	41.4

Table. A-58. Experimental data and SR files code.

Parameters	Temperature, °C	Humidity, %	Wind speed, km/h
	30	67	5
Chemicals	Composition, g	SR file number	Chemical temperature
Lauric acid	3	1101	38.5
Stearic acid	3	1102	39.4
Paraffin wax	3	1103	44.6
Lauric acid	2	1104	42.7
Stearic acid	2		
Control	Nil.	1105	36.9

Table. A-59. Experimental data and SR files code.

Parameters	Temperature, °C	Humidity, %	Wind speed, km/h
	30	66	5
Chemicals	Composition, g	SR file number	Chemical temperature
Lauric acid	3	1106	39.5
Stearic acid	3	1107	34.7
Paraffin wax	3	1108	45.6
Lauric acid	2	1109	38.9
Stearic acid	2		
Control	Nil.	1110	42.6

Table. A-60. Experimental data and SR files code.

Parameters	Temperature, °C	Humidity, %	Wind speed, km/h
	30	66	5
Chemicals	Composition, g	SR file number	Aluminium temperature
Lauric acid	3	1111	41.4
Stearic acid	3	1112	33.6
Paraffin wax	3	1113	48.1
Lauric acid	2	1114	34.5
Stearic acid	2		
Control	Nil.	1115	43.8

Table. A-61. Experimental data and SR files code.

Parameters	Temperature, °C	Humidity, %	Wind speed, km/h
	31	64	6
Chemicals	Composition, g	SR file number	Aluminium temperature
Lauric acid	3	1116	31
Stearic acid	3	1117	37.5
Paraffin wax	3	1118	36.3
Lauric acid	2	1119	41.5
Stearic acid	2		
Control	Nil.	1120	45.5

Table. A-62. Experimental data and SR files code.

Parameters	Temperature, °C	Humidity, %	Wind speed, km/h
	31	64	6
Chemicals	Composition, g	SR file number	Aluminium temperature
Lauric acid	3	1121	40.4
Stearic acid	3	1122	30.4
Paraffin wax	3	1123	30.4
Lauric acid	2	1124	40.1
Stearic acid	2		
Control	Nil.	1125	43.7

Table. A-63. Experimental data and SR files code

Parameters	Temperature, °C	Humidity, %	Wind speed, km/h
	31	66	6
Chemicals	Composition, g	SR file number	Aluminium temperature
Lauric acid	3	1131	33.6
Stearic acid	3	1132	36.2
Paraffin wax	3	1133	48.1
Lauric acid	2	1134	50.3
Stearic acid	2		
Control	Nil.	1135	47.6

Table. A-64. Experimental data and SR files code.

Parameters	Temperature, °C	Humidity, %	Wind speed, km/h
	31	66	6
Chemicals	Composition, g	SR file number	Aluminium temperature
Lauric acid	3	1136	37.3
Stearic acid	3	1137	30.8
Paraffin wax	3	1138	48.3
Lauric acid	2	1139	38.2
Stearic acid	2		
Control	Nil.	1140	40.1

Table. A-65. Experimental data and SR files code.

Parameters	Temperature, °C	Humidity, %	Wind speed, km/h
	31	67	6
Chemicals	Composition, g	SR file number	Aluminium temperature
Lauric acid	3	1141	46.5
Stearic acid	3	1142	39.2
Paraffin wax	3	1143	47.2
Lauric acid	2	1144	44.5
Stearic acid	2		
Control	Nil.	1145	33.8

Table. A-66. Experimental data and SR files code.

Parameters	Temperature, °C	Humidity, %	Wind speed, km/h
	31	63	8
Chemicals	Composition, g	SR file number	Aluminium temperature
Lauric acid	3	1151	41.2
Stearic acid	3	1152	45
Paraffin wax	3	1153	45.3
Lauric acid	2	1154	43.9
Stearic acid	2		
Control	Nil	1155	48.3

Table. A-67. Experimental data and SR files code.

Parameters	Temperature, °C	Humidity, %	Wind speed, km/h
	31	63	8
Chemicals	Composition, g	SR file number	Aluminium temperature
Lauric acid	3	1156	51.5
Stearic acid	3	1157	52.5
Paraffin wax	3	1158	41
Lauric acid	2	1159	46.9
Stearic acid	2		
Control	Nil.	1160	45

Table. A-68. Experimental data and SR files code.

Parameters	Temperature, °C	Humidity, %	Wind speed, km/h
	31	63	8
Chemicals	Composition, g	SR file number	Aluminium temperature
Lauric acid	3	1156	51.5
Stearic acid	3	1157	52.5
Paraffin wax	3	1158	41
Lauric acid	2	1159	46.9
Stearic acid	2		
Control	Nil.	1160	45